

HARRAN ÜNİVERSİTESİ MÜHENDİSLİK DERGİSİ

HARRAN UNIVERSITY JOURNAL of ENGINEERING

e-ISSN: 2528-8733 (ONLINE)

URL: http://dergipark.gov.tr/humder

5G Yüksek Frekanslı Algılama Uygulamaları için Esnek Ara Bağlantı ve Toprak Kusurlu Bölünmüş Halka Rezonatörün Sayısal Analizi

Numerical Analysis of a Flexible Interconnect and Ground-Defected Split Ring Resonator for High-Frequency 5G Sensing Applications

Yazar(lar) (Author(s)): Ekrem ALTINÖZEN¹

¹ORCID ID: 0000-0003-3671-6732

Bu makaleye şu şekilde atıfta bulunabilirsiniz (To cite to this article): Altınözen E., "5G Yüksek Frekanslı Algılama Uygulamaları için Esnek Ara Bağlantı ve Toprak Kusurlu Bölünmüş Halka Rezonatörün Sayısal Analizi", Harran Üniversitesi Mühendislik Dergisi, 10(3): 172-183, (2025).

DOI: 10.46578/humder.1741743



Harran Üniversitesi Mühendislik Dergisi

Harran University Journal of Engineering





Research Article

5G Yüksek Frekanslı Algılama Uygulamaları için Esnek Ara Bağlantı ve Toprak Kusurlu Bölünmüş Halka Rezonatörün Sayısal Analizi

Ekrem ALTINÖZEN^{1*}, D

¹Elektrik-Elektronik Mühendisliği Bölümü, Mühendislik Fakültesi, Harran Üniversitesi, Şanlıurfa, Türkiye

Makale Bilgisi

Başvuru: 14/07/2025 Düzeltme: 21/07/2025 Kabul: 21/07/2025 Yayınlanma: 30/09/2025

Alıntı

Yüksek Frekanslı Algılama Uygulamaları için Esnek Ara Bağlantı ve Toprak Kusurlu Bölünmüş Halka Rezonatörün Sayısal Analizi", Harran Üniversitesi Mühendislik Dergisi, 10(3): 172-183, (2025).

Öz

Giyilebilir kablosuz iletisim ve biyomedikal uygulamaların artması, kullanıcıların sağlık ve zindelik takibini önemli ölçüde geliştirmek ve insan-makine arayüzlerinin etkileşim performansını artırmak için konformal elektroniklere olan ihtiyacı doğurmuştur. Bu makale, polimer kompozitler temel alınarak geliştirilen, toprak düzleminde kusur içeren bölünmüş halka rezonatörlü (Defected Ground Split Ring Resonator - DGS SRR) ve hafif, uyumlu Radyo Frekansı (RF) bağlantı elemanlarının sayısal karakterizasyonunu açıklamaktadır. Kullanılan malzeme, Polidimetilsiloksan (PDMS) adlı bir polimerdir. Konformal bükülmenin, RF bağlantı elemanlarının elektromanyetik performansı üzerindeki etkisi, frekans alanında Sonlu Elemanlar Yöntemi (FEM) ile analiz edilmiştir. Elektromanyetik performansın avantajları, yansıma katsayıları ile birlikte doğruluk ve çok yönlülük açısından tartışılmış ve sonuçlar karşılaştırılmıştır. Simülasyon modeliyle tasarlanan esneyebilir yüksek frekanslı mikroşerit bağlantı elemanları, maksimum -15 dB S₁₁ büyüklüğüne ve minimum -0.62 dB S21 yansıma katsayısı büyüklüğüne sahiptir. Bölünmüş Halka Rezonatör (SRR), sub-milimetre 5G frekans bandı içerisinde 3.46 GHz'de rezonansa girerek, -24.45 dB'lik bir yansıma katsayısı (S11) zirvesi sergilemektedir; bu da güçlü bir rezonans ve verimli enerji bağlantısını göstermektedir. Sunulan mikroşerit iletim hattı, giyilebilir mikroşerit sensörlerin besleme ağı için ve mekanik esnekliğin kaçınılmaz olduğu uygulamalarda, RF algılama sistemlerinin güvenilirliğini ve dayanıklılığını artırmak için faydalı bir örnektir.

Anahtar Kelimeler: Esnek Rezonatör, Bükülme Bozulması, 5G Uygulamaları

Numerical Analysis of a Flexible Interconnect and Ground-Defected Split Ring Resonator for High-Frequency 5G Sensing Applications

Article Information

Received: 14/07/2025 Revised: 14/07/20225 Accepted: 21/07/2025 Published: 30/09/2025

Citation

Altınözen E., "Numerical Analysis of a Flexible Interconnect and Ground-Defected Split Ring Resonator for High-Frequency 5G Sensing Applications", *Harran University Journal of Engineering*, 10(3): 172-183, (2025).

Abstract

The increasing number of wearable wireless communication and biomedical applications have led to need for conformal electronic to significantly enhance health and wellness monitoring of users and performance of improve interaction human-machine interfaces. This paper describes numerical characterization conformal and light-weight Radio Frequency (RF) interconnects with ground defected split ring resonator based upon polymer composites Polydimethylsiloxane, namely PDMS, is used. The impact of conformal bending on the electromagnetic performance of the RF interconnects was considered and analyzed in frequency domain Finite Element Modelling method, (FEM). The merits of electromagnetic performance reflection coefficients, in conjunction with accuracy, and versatility are discussed, and results are compared. Simulated model the designed stretchable high-frequency microstrip interconnects has a maximum magnitude, S₁₁ of -15 dB and a minimum magnitude of reflection coefficient, S₂₁ of -0.62 dB. The Split Ring Resonator (SRR) exhibits resonance within the sub-millimeter 5G frequency band, achieving a resonant frequency at 3.456 GHz with a peak reflection coefficient (S₁₁) of -24.45 dB, indicating strong resonance and efficient energy coupling. The presented microstrip transmission line is a useful example for feeding network of wearable microstrip sensors and in applications where inevitable mechanical flexibility helps improve reliability and durability of RF sensing systems.

Keywords: Flexible Resonator, Bending Deformation, 5G Applications

*İletişim yazarı, e-mail: ekremaltinozen@harran.edu.tr

*Corresponding author, e-mail: ekremaltinozen@harran.edu.tr

DOI: 10.46578/humder.1741743

1. INTRODUCTION

The market for wearable electronic devices has experienced substantial growth in recent years. To enhance user comfort and enable seamless integration with the human body, these devices must be mechanically flexible, allowing them to deform in response to body movements [1-6]. With the rapid advancement of functional materials and fabrication technologies, wearable sensors have become integral to human—machine interfaces and real-time health monitoring systems [7-10]. Unlike conventional rigid wired devices, which offer limited conformability for long-term monitoring, flexible sensors minimize interference with daily activities and are well-suited for integration into 5G-enabled systems [7-10].

Wireless communication is typically employed to transmit data from wearable devices to remote platforms such as smartphones. To ensure reliable system performance and regulatory compliance (e.g., CE certification), it is essential to thoroughly characterize the behavior of sensors and interconnects under realistic operating conditions. Compared to traditional rigid electronics, flexible systems demand more extensive testing and simulation to verify their functionality across a wide range of deformation scenarios encountered during their operational lifespan [11, 12]. As a result, the capabilities of electromagnetic simulation tools play a critical role in the development of such devices.

While several studies have explored the design of flexible interconnects using elastomeric substrates, most have focused on low-frequency or direct current (DC) applications [13, 14]. In contrast, flexible microstrip lines operating at higher frequencies and featuring transverse discontinuities—such as bends or abrupt changes in width—can induce transverse currents that are likely to excite transverse electric (TE) surface wave modes [15]. These modes can result in unwanted electromagnetic coupling with adjacent structures and increased power loss. Therefore, accurate modeling of flexible microstrip devices requires full-wave simulations of the entire system, rather than relying solely on quasi-TEM approximations. This presents a significant computational challenge, necessitating precise representation of electromagnetic field distributions within the deformed structures [16, 17].

One of the fundamental challenges in the design of wearable sensors is that sensors are typically developed as planar structures. However, in real-world applications, these components are subject to various mechanical deformations [11, 12]. The impact of such deformations is most investigated through experimental methods, often by modeling the antenna as being bent along a cylindrical surface[18, 19]. Although less frequently, numerical simulations using commercial electromagnetic solvers have also been employed to analyze these effects [20, 21].

In our previous work, we addressed complex two-dimensional geometrical deformations in transmission lines and antennas using a Green Coordinates-based geometry morphing technique, combined with an Unstructured Transmission Line Modeling (UTLM) approach and an in-house geometry kernel, mesher and solvers [22, 23]. The *finite element* (FE) [24], *finite difference time domain* (FDTD) [25] are techniques used to solve electromagnetic problems and can be used to design and characterize passive RF components including antennas. The selected simulation must provide realistic geometric modelling of bending, twisting, warping and crumpling that a device will undergo when worn whilst ensuring efficient use of computer memory to ensure the final device can be simulated. Bending microstrip interconnects and circuits since they are used to guide signals from one component to another and characterization of their performance is necessary to understand system performance and possible coupling effect which can lead to interference [17]. sensor designs will inevitably generate non-coordinate aligned geometry elements. The discretization of the object using an unstructured conformal mesh is an important step for reducing discretization errors for a given memory requirement.

In the present study, we extend this investigation with Finite Element Modelling method without coaxial cable excitation to previously unexplored deformation scenarios, such as cylindrical concave and convex bending, and concave bending of transmission lines and analyze the performance variations of split-ring

resonators under such extreme bending conditions. To obtain the simulation results, we employed a frequency-domain *Finite Element Method* (FEM), which solves the electromagnetic problem at discrete frequency points. Consequently, generating a complete frequency response requires repeating the analysis across the desired frequency range. Although a time-domain FEM approach could be used to capture nonlinear effects, it typically demands significantly more memory due to the additional computational overhead involved.

This work concentrates on the comparison of performance of flexible transmission line and split ring resonator techniques when modelling deformations typically seen in wearable devices. Consequently, simulations will be restricted to modelling 50 Ω microstrip interconnects which are geometrically simpler than other passive devices like antennas. Microstrip interconnects, however, have an important role in RF.

The subsequent part of this paper is organized as follows. Section 2 introduces the geometric modeling of high-frequency interconnects within a simulation environment, with particular emphasis on the structural configuration of flexible interconnects and a comparative analysis of results obtained without the use of coaxial cables. Section 2 investigates the influence of bending conditions on the scattering parameters of the interconnect under various deformation scenarios. Section 3 extends this analysis to examine the effects of bending on the scattering behavior of split-ring resonators (SRRs) within the same simulation framework. Finally, Section 4 summarizes the key findings and conclusions drawn from this study.

2. GEOMETRIC MODEL OF FLEXIBLE INTERCONNECTS

Figure 1(a) defines the geometry of the undeformed microstrip transmission line simulated in this study. The microstrip line has a width of W = 2.5 mm and a length of L = 50 mm, fabricated on a substrate with dimensions $L_{sub} = 50$ mm and $W_{sub} = 25$ mm. The substrate has a thickness of 1 mm, a relative permittivity of $\varepsilon_r = 2.77$, and a loss tangent of $\tan \delta = 0.01$. The metallic trace has a thickness of 0.1 mm. The ground-plane-integrated defected split-ring resonator (DSRR) features the following dimensions: $w_s = 1.7$ mm, $L_h = 9.5$ mm, $L_v = 9.5$ mm, g = 1.5 mm, and g = 7.2 mm. The microstrip size was chosen to be consistent with previous experimental work of [26] who used the polymer PDMS as a substrate and [27, 28] who measured the dielectric constant of PDMS. The characteristic impedance of the microstrip was 52 Ω . Initially, coaxial cables at each end of the microstrip were used to excite the transmission line because (1) this is the most likely experimental set up and (2) the electromagnetic modes are confined to the interior of the cable and allow the extraction of S_{11} and S_{21} without making assumptions on the physical truncation of the mode.

In later simulations, the microstrip TE mode is used to extract S_{11} and S_{21} . This was necessary because the geometric deformation algorithm also deforms the coaxial cable from its circular analytical form. The split ring geometry in reference [29] has adapted for flexible substrate with microstrip transmission excitation for this application (See Figure 1(b)).

The simulation boundaries in FEM limited the region to be meshed and simulated. All boundaries are assumed to be Absorbing Boundary Conditions (ABC). ABC boundaries are placed 30 mm from the top and the bottom of the transmission line structure. There is no gap between the edge of substrate length side and computation box. The computational box is not shown in Figure 1.

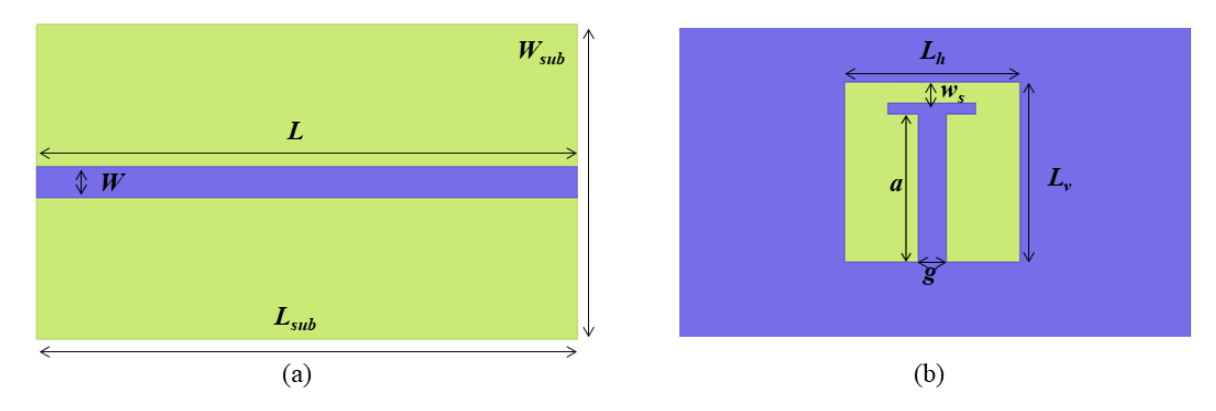


Figure 1. The geometry of the microstrip transmission line and the split-ring resonator (SRR) employed in this study is illustrated schematically (not to scale).

The simulation technique has a simple method of exciting the transmission line and extracting the reflection (S_{11}) and transmission coefficients S_{21} . For simulations, the mesh is generated using an adaptive meshing technique with a fixed frequency of 5 GHz and a maximum of 20 adaptive passes with an adaptive refinement factor $\Delta s = 0.02$. The grid is constrained to a size between $\lambda/15$ and maximum 20 iterations adjusted to provide smaller value than Δs . For flat transmission line case, an open boundary condition has been applied for computational box. As noted earlier; to obtain the frequency response, the solver needs to sweep the frequency. A fixed discrete sweep with 401 points between 1 GHz and 10 GHz was used. A selected iterative solver was used for simulations with a residual tolerance of 10^{-9} and the 2^{nd} order basis options were selected for higher accuracy. The solver required between 50 to 60 iterations to meet the required accuracy, where λ is 60 mm, free space wavelength at 5 GHz. Meshing applied length constraint ($\lambda/15$) whole computation box, with grid refinement factor 4 and a single frequency adaptive meshing respectively.

The S-parameters S_{11} and S_{21} obtained from simulations are shown in Figure 2. S_{21} is close to 0 dB, especially below 5 GHz, which shows the interconnect has little loss. Above 5 GHz, the loss increases slightly. Ignoring, for the moment, the resonant dips, S_{11} is initially low but increases with frequency indicating a growing mismatch between the transmission line and the coaxial cable. The mismatch between the mode within the coaxial and the microstrip will generate a reflection at the boundary which causes the resonant dips in S_{11} . The dip positions are dependent on the phase of the reflection at the coaxial microstrip interface. Since the dips occur at different frequencies, the phase of reflection at this boundary is different for the two analysis techniques. This is not unexpected because the underlying approximations and meshes are different. As the frequency increases above 5 GHz, the meshing errors will increase. This leads to larger reflections at the coaxial / interconnect boundary as well as greater coupling to higher order modes resulting in an increase S_{11} and a decrease in S_{21} (more loss).

Although coaxial feeds are more realistic, the interpretation of the results is not as straight forward because it is difficult to isolate the effects of the coaxial feed and the deformed microstrip. Consequently, the microstrip is exciting directly using quasi-TEM mode.

The dielectrics used in the simulation were assumed to be lossy and the metal was assumed to be a perfect conductor. In addition, any changes in dielectric properties induced by stress in the polymer caused by bending are ignored. Consequently, any increase in loss observed in these simulations is solely caused by deformation.

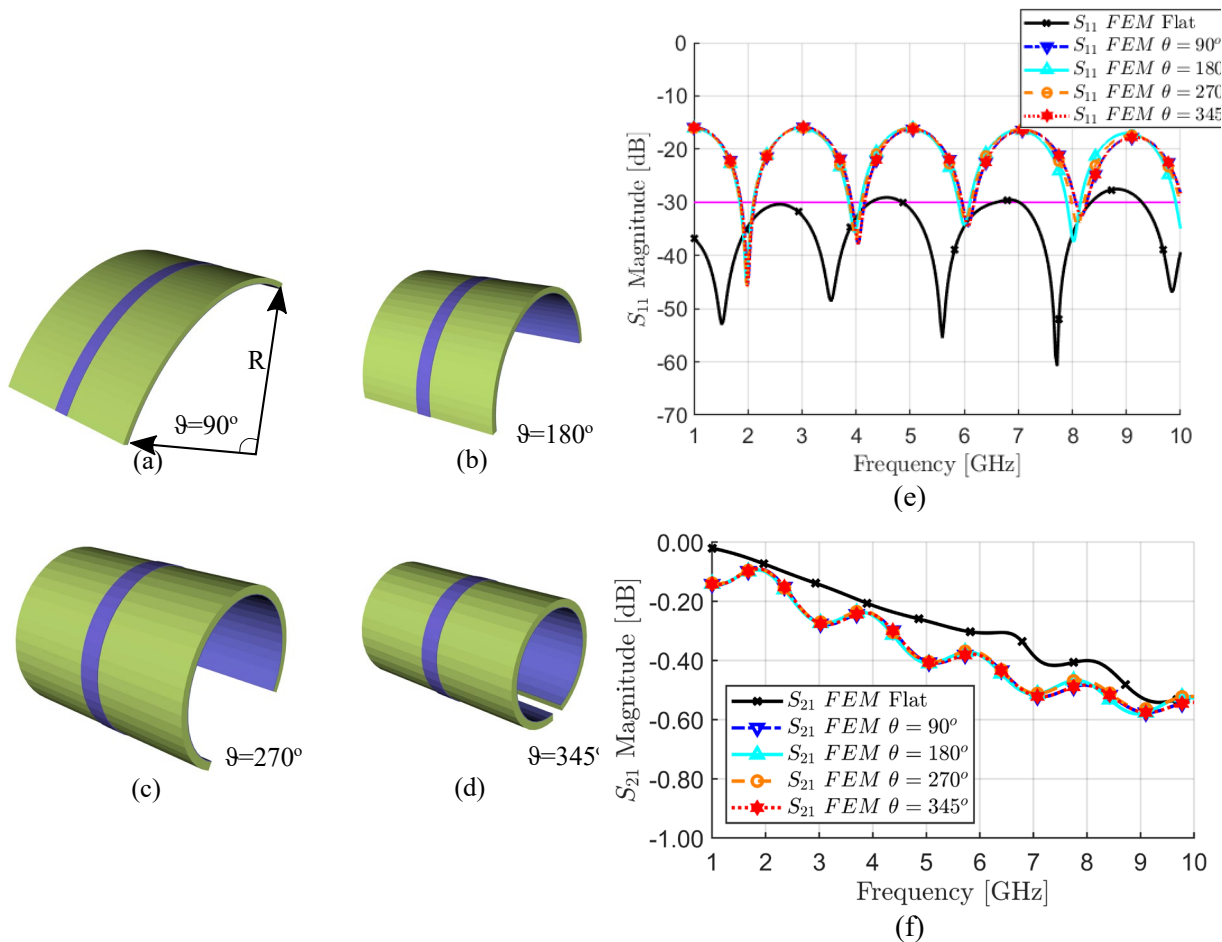


Figure 2. Cylindrically bent transmission lines were analyzed for bending angles of (a) 90°, (b) 180°, (c) 270°, and (d) 345°, respectively. The corresponding FEM simulation results are presented in terms of (e) S_{11} and (f) S_{21} , evaluated across the bending angles ranging from $\theta = 90^{\circ}$ to $\theta = 345^{\circ}$.

	Table 1.	Bending	Angle	and Radius
--	----------	---------	-------	------------

Table 1. Defiding / Highe and Radius					
Bending Angle (°)	Bending Radius (mm)				
90	32				
180	16				
270	11				
345	8.3				

To understand the effect of bending on the propagation of a wave along the microstrip simulations, the phase length of the transmission lines needs to be constant. If the propagation coefficient does not change appreciably under bending, this condition will also apply to the physical length. Because of keeping the length constant, any increase in loss can be attributed to the bending of the transmission line. The boundaries of the deformed transmission line are defined analytically. Two related parameters can be used to express the degree of bending: the bending angle θ and the bending radius. In this work, the bending angle has been used and varied from 90° flat case to 345° which is an extremely curved case. The four cases are shown in Figure 2(a)-(d). Table 1 can be used to convert the bending angle to bending radius. S_{11} -results are below -30 dB across the simulated frequency range for all deformed transmission lines. Again, there are resonant dips, and the separation of the dips do not change significantly on bending.

In terms of S_{21} , simulation results have slightly increased loss at higher frequencies when the bend angle increases beyond 180° bend angle. Even in the case of extreme bending, the increase in loss is ~ 0.1 dB. The slightly higher loss in the case makes it harder to extract a concrete value but it is likely to be of the same order. For the second set of simulations, the bending axis was parallel to the transmission line (see

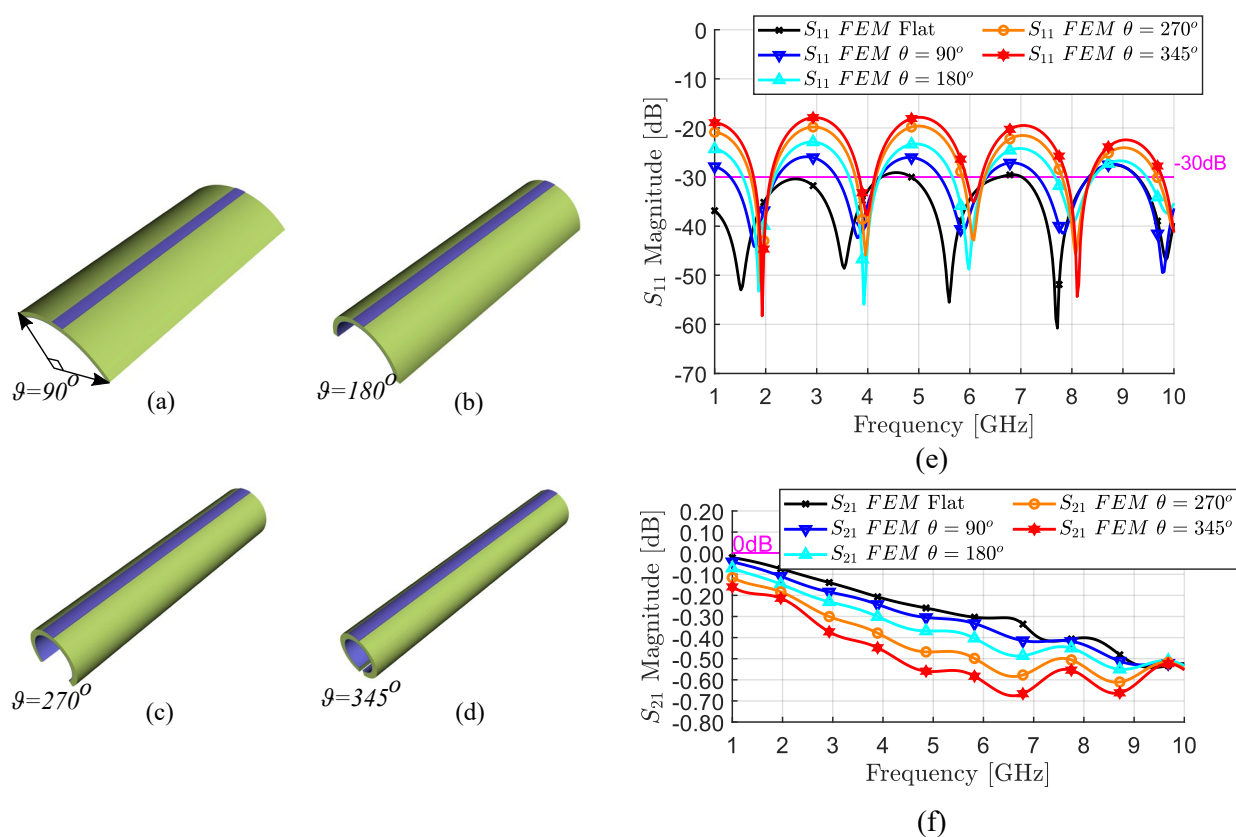


Figure 3. Cylindrically bent transmission lines were analyzed for bending angles of (a) 90°, (b) 180°, (c) 270°, and (d) 345°, respectively. The corresponding FEM results are presented in terms of (e) S_{11} and (f) S_{21} , evaluated across the bending angles ranging from $\theta = 90^{\circ}$ to $\theta = 345^{\circ}$.

Table 2. Bending Angle and Radius				
Bending Angle (°)	Bending Radius (mm)			
90	16			
180	8			
270	5.5			
2/15	12			

Figure 3(a)-(d)). Again, the physical length of the line was held fixed. The same bending angles were used but because the width of the microstrip is smaller than the length, the bend radius will be smaller for a given bend angle. Table 2 can be used to convert the bending angle to bending radius.

For simulation, S_{11} increases from below -30 dB to \sim -18 dB (see Figure 3(e)). For simulation results, the location of the resonant dips and their separation is independent of the bend angle. There is some variability in both the location and separation of the resonant dips. Similar results are found for simulation but there is a clear trend of more loss at higher frequency as the bend angle increases. (See Figure 3(f).) The small difference probably reflects the different methods of finding the excitation mode.

A more realistic bending would be a 90° bend at the center of the transmission line. The bending can be external or internal. Initially, an external bend is considered, and the four cases considered are shown in Figure 4(a)-(d). The geometry is constructed with piecewise polygonal tube which allows the generation of a geometry without unphysical gaps.

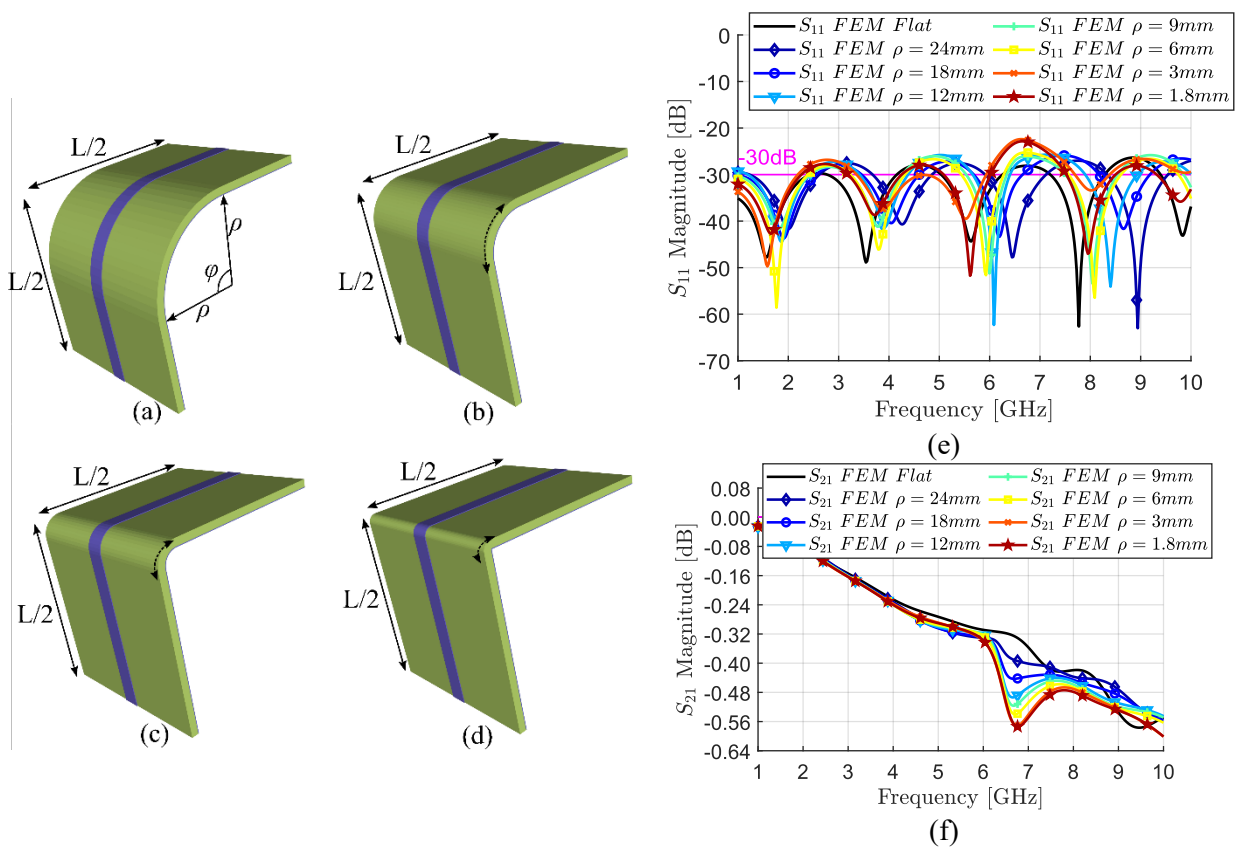


Figure 4. Flexible interconnects with minimum bending arc radii of (a) 24 mm, (b) 6 mm, (c) 3 mm, and (d) 1.2 mm were investigated. FEM results are presented in terms of the (e) S₁₁ and (f) S₂₁, corresponding to minimum bending arc lengths ranging from 24 mm to 1.2 mm.

According to Fig. 4 (e), the reflection coefficient S₁₁ is generally below the -25 dB. The bend at the center of the transmission line will cause additional reflections which make the analysis of the position and separation not meaningful and have been omitted. Simulation results show an increase in loss as the frequency is increased, both sets of results have a small amount of additional loss centered around 6.7 GHz.

This loss increases with a bend radius. At a bend radius of 1.2 mm the additional loss is 0.1 dB. The addition loss may be associated with increased radiation loss associated with a very weak resonant mode caused by the reflection at the bend and imposition of the boundary conditions. Simulations have also been performed on a similar structure with the bend in the opposite direction forming an inner corner. Similar conclusions were found apart from the additional loss of 6.7 GHz which was absent.

3. MODEL OF DEFORMED FLEXIBLE SPLIT RING RESONATOR

Deformation of the resonator element inevitably leads to a shift in the resonance frequency and degradation in performance metrics. To evaluate the real-world, in situ behavior of the structure under mechanical stress, we applied controlled deformation to a transmission line integrated with a split-ring resonator (SRR) positioned beneath it. As a baseline for comparison, planar (undeformed) configurations of the microwave sensing element were first simulated. In the planar case, the structure with a ground-plane defected SRR exhibited a resonance at 3.46 GHz with a reflection coefficient $S_{11} = -24.47$ dB, while the transmission coefficient S_{21} showed a pronounced dip at 3.82 GHz with a minimum of -20.72 dB.

3.1 Cylindrical Bending Along the Width of SRR

This section investigates the impact of cylindrical bending on the performance of a split-ring resonator (SRR). Initially, the planar configuration of the SRR was modeled using Boolean geometry operations. Subsequently, controlled deformations were introduced by varying the bending angle, as detailed in Table 2. Figure 5 illustrates the influence of these deformations on the resonant frequency of the SRR.

Figure 5(a) presents the simulated reflection coefficient (S_{11}) as a function of frequency. The insets depict the deformed SRR geometries corresponding to cylindrical bending angles of $\theta = 90^{\circ}$, 180° , 270° , and 345° , respectively (see Figure 5(a)–(b)). The results indicate a gradual downward shift in the resonant frequency with an increasing bending angle. Notably, in all cases, the S_{11} value at resonance remains below -20 dB, as shown in Figure 5(a). For the maximum bending angle of 345° , the resonant frequency shifts by approximately 3.34%, with only a slight degradation in the S_{11} peak (approximately -1 dB).

Regarding the transmission coefficient (S_{21}), the resonance dip shifts by about 1.35%, accompanied by an improvement of approximately 3 dB. This effect is more pronounced when bending occurs along the length of the SRR. In contrast, bending along the width results in a smaller frequency shift due to the compensating influence of fringing fields at the radiating edges, which mitigate the effective length reduction. Figure 5(b) illustrates the impact of cylindrical bending along the width of the SRR on the S_{21} parameter. In this case, the resonance dip remains relatively stable, while the stopband depth increases by approximately 4 dB.

3.2 Cylindrical Bending Along the Length of SRR

This section examines the impact of cylindrical deformation applied along the width of the transmission line. The deformed geometries used in the analysis are shown in the insets of Figure 6(a)–(d). The effect of this deformation on the resonant frequency is compared to the planar (undeformed) case, as illustrated in Figure 6. The shaded region in the figure highlights the 10 dB fractional bandwidth range.

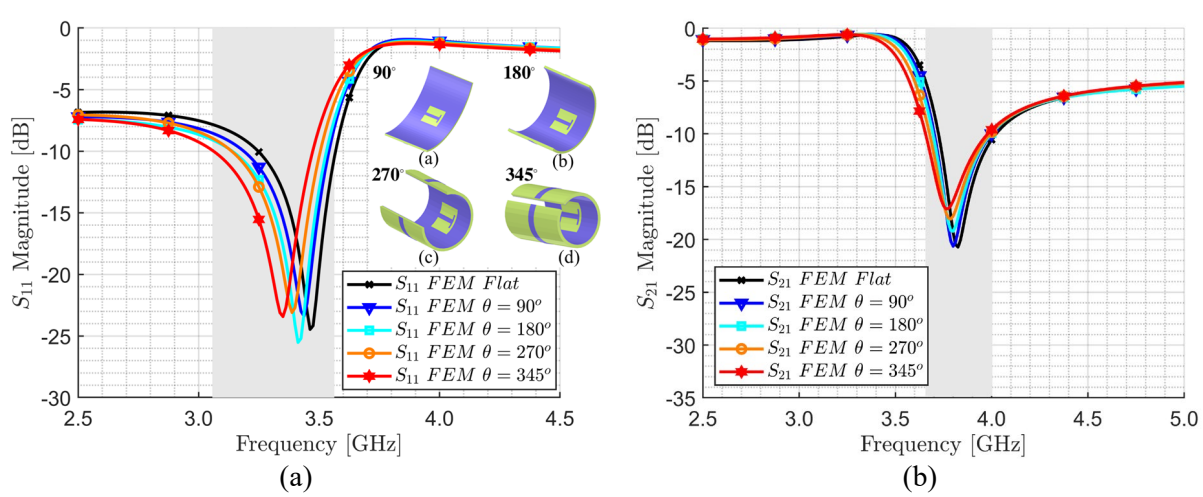


Figure 5. A cylindrically bent transmission line incorporating a defected split-ring resonator (SRR) structure along its longitudinal axis was investigated. The inset illustrations depict deformation angles of (a) 90°, (b) 180°, (c) 270°, and (d) 345°, respectively. FEM results are presented in terms of (a) S₁₁ and (b) S₂₁, corresponding to bending angles ranging from $\theta = 90^{\circ}$ to $\theta = 345^{\circ}$.

The results indicate that cylindrical bending along the width axis has a more pronounced detrimental effect on the resonant frequency than bending along the length, with a maximum frequency shift of approximately 7.78%. This behavior can be attributed to the mechanical deformation by reducing the effective electrical length of the resonator when bent inward along the width. In contrast, bending along the length axis allows fringing fields at the resonator's edges to increase the effective length, thereby lowering the resonant frequency.

The influence of width-wise deformation on the transmission coefficient (S₂₁) is presented in Figure 6(b), which compares the S₂₁ response of the planar resonator with those of the deformed configurations. It is evident that cylindrical deformation along the width significantly alters the band-stop characteristics, shifting the resonance dip to higher frequencies by approximately 6.44% and increasing the stopband depth

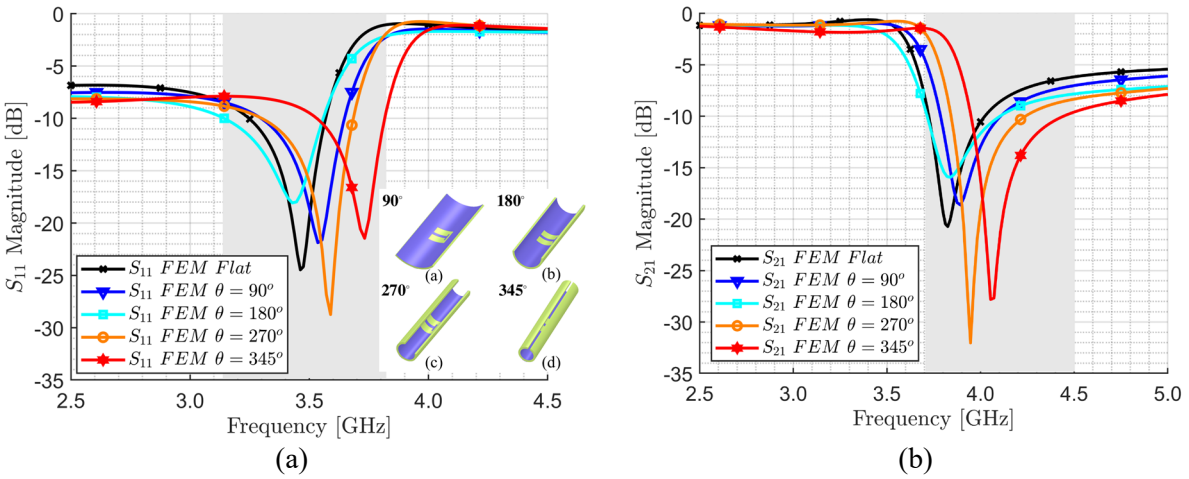


Figure 6. A cylindrically bent transmission line integrated with a defected split-ring resonator (SRR) structure along the transverse axis was analyzed. The inset illustrations depict deformation angles of (a) 90°, (b) 180°, (c) 270°, and (d) 345°, respectively. FEM results are presented in terms of (a) S_{11} and (b) S_{21} , corresponding to bending angles ranging from $\theta = 90^{\circ}$ to $\theta = 345^{\circ}$.

3.3 Folding Deformation

In this section explores the effects of folding deformation on the performance of the antenna structure. Folding was introduced by applying arc-radius warping along the ground plane, centered on the transmission line. The resulting shift in resonant frequency due to folding deformation is compared to the flat (undeformed) case, as illustrated in Figure 7. The inset figures (Figure 7(a)–(d)) show the deformed geometries corresponding to various arc radii.

As shown in Figure 7(a), decreasing the folding arc radius results in a resonant frequency shift of up to approximately 11.48% in the reflection coefficient (S₁₁). This behavior suggests that folding along the center of the split-ring resonator increases its effective electrical length, thereby lowering the resonant frequency. The shaded region in the figure highlights the 10 dB bandwidth variation, indicating a reduction in bandwidth to around 3.1 GHz for the deformed resonator. In all cases, the S₁₁ magnitude at resonance decreases, with the most significant degradation observed for center folding along the length of the resonator. Figure 7(b) presents the corresponding transmission coefficient (S₂₁) results. Compared to S₁₁, the impact of center folding on S₂₁ is less pronounced. However, a noticeable shift in the band-stop region is still observed.

Table 3 summarizes the effects of various deformation types—including cylindrical bending along the width and length, as well as center folding—on S₁₁ and S₂₁ characteristics. Among these, center folding exhibits the most significant impact on both the resonant frequency and peak values of S₁₁ and S₂₁. Cylindrical deformation along the length also causes substantial frequency shifts, while deformation along the width has the least effect.

From a sensing perspective, structural modifications such as lengthwise bending and center folding offer a broader frequency tuning range, which may enhance sensing resolution. However, the relationship between deformation and frequency shift is nonlinear. This nonlinearity suggests that machine learning-based frequency classification techniques may be necessary to accurately characterize and predict sensor responses under varying deformation conditions.

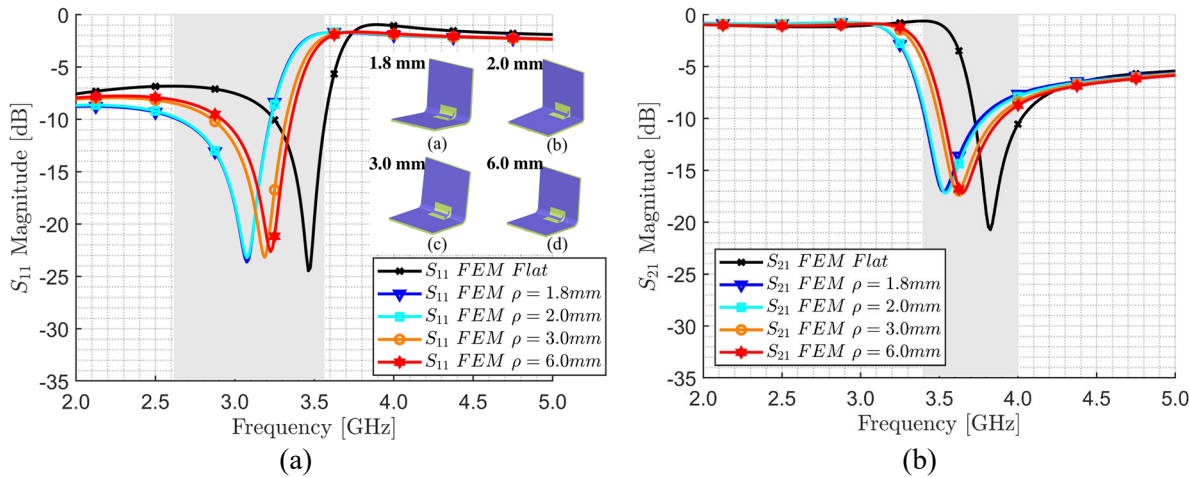


Figure 7. A folded transmission line incorporating a defected split-ring resonator (SRR) structure at its center was examined under varying bending arc radius. The inset illustrations depict bending arcs of (a) 1.8 mm, (b) 2.0 mm, (c) 3.0 mm, and (d) 6.0 mm, respectively. FEM results are presented in terms of (a) S_{11} and (b) S_{21} , corresponding to bending arc radii ranging from $\rho = 1.8$ mm to $\rho = 6$ mm.

Table 3. Numerical Investigation of the Effects of Bending Deformation on the S₁₁ and S₂₁ Parameter and Resonant Frequency Shift

Deformation		Min (S ₁₁)	Δ(f) (%)	Min (S ₂₁)	Δ(f) (%)
		dB		dB	
Bending Width Angle	90	-24.46	0.72	-20.64	0.65
(°)	180	-25.52	1.44	-19.23	0.65
	270	-23.09	2.16	-18.07	0.98
	345	-23.42	3.24	-17.08	1.30
Bending Length Angle	90	-21.87	2.11	-18.62	1.91
(°)	180	-18.07	0.97	-15.93	0.37
	270	-28.73	3.66	-32.03	3.17
	345	-21.45	7.78	-27.67	6.44
Folding Arc Radii	6.0	-22.63	6.85	-17.17	4.83
(mm)	3.0	-23.18	7.94	-17.02	5.55
	2.0	-22.77	11.48	-17.02	7.84
	1.8	-23.63	11.19	-17.02	7.51

Our numerical experiments demonstrate strong agreement with the findings of Khaleel et al. (2012) for frequency selective surface (FSS) structures. While their study is limited to two bending radii, our work extends this by systematically exploring a broader range of deformation conditions for single split-ring resonators (SRRs), highlighting their potential as strain or bend-aware sensors.

4. CONCLUSION

This study explores the influence of mechanical deformations on a practical ground-plane defected splitring resonator (DSRR) fabricated on a PDMS substrate, designed to operate within the sub-6 GHz 5G frequency band. A diverse set of one-dimensional (1D) deformation scenarios were systematically applied to assess their impact on the resonator's electromagnetic performance.

The findings reveal that the flexible transmission line maintains a relatively stable loss of insertion across different bending conditions. However, notable variations in the reflection coefficient (S_{11}) are observed,

particularly under cylindrical bending along both the length and width axes. Deformation along the width of the transmission line, with the resonant element positioned beneath, results in a significant downward shift in the resonant frequency. This effect is especially pronounced when the deformation is centered on the sensing element, as it alters the effective electrical length of the resonator.

Folding deformation, especially when applied at the center of the SRR, has a marked impact on the transmission coefficient (S_{21}), producing the largest observed shift in resonance frequency. Among all deformation types, center folding exhibits the most substantial influence on both S_{11} and S_{21} characteristics. Importantly, even under the most severe deformation scenarios, the resonant element continues to operate within the designated sub-6 GHz 5G band. This resilience highlights the potential of such flexible resonator designs for robust sensing and communication applications in mechanically dynamic environments.

CONFLICT OF INTEREST

The authors declare that they have no known competing financial interests or personal relationships that could have appeared to influence the work reported in this paper.

STATEMENT OF PUBLICATION ETHICS

We declare that all stages of the study comply with research and publication ethics, and that we have adhered to ethical principles and scientific citation standards.

AUTHOR STATEMENT

Ekrem ALTINÖZEN: Writing – original draft, Visualization, Software, Methodology, Data curation, Conceptualization

REFERENCES

- [1] J. Chen *et al.*, "Polydimethylsiloxane (PDMS)-Based Flexible Resistive Strain Sensors for Wearable Applications," *Applied Sciences*, vol. 8, no. 3, 2018.
- [2] M. Amjadi, K.-U. Kyung, I. Park, and M. Sitti, "Stretchable, Skin-Mountable, and Wearable Strain Sensors and Their Potential Applications: A Review," *Advanced Functional Materials*, vol. 26, no. 11, pp. 1678-1698, 2016.
- [3] C. Pang *et al.*, "A flexible and highly sensitive strain-gauge sensor using reversible interlocking of nanofibres," *Nat Mater*, vol. 11, no. 9, pp. 795-801, Sep 2012.
- [4] C. M. Lochner, Y. Khan, A. Pierre, and A. C. Arias, "All-organic optoelectronic sensor for pulse oximetry," *Nat Commun*, vol. 5, p. 5745, Dec 10 2014.
- [5] Z. Chen, J. Xi, W. Huang, and M. M. F. Yuen, "Stretchable Conductive Elastomer for Wireless Wearable Communication Applications," *Sci Rep*, vol. 7, no. 1, p. 10958, Sep 8 2017
- [6] S. C. Mukhopadhyay, Wearable electronics sensors: For safe and healthy living. Springer, 2015.
- [7] B. Yan, F. Zhang, M. Wang, Y. Zhang, and S. Fu, "Flexible wearable sensors for crop monitoring: a review," *Front Plant Sci*, vol. 15, p. 1406074, 2024.
- [8] A. Mostaccio, G. Antonelli, R. Capuano, C. D. Natale, E. Martinelli, and G. Marrocco, "Full-LIG Wireless Batteryless Flexible Sensor for the Detection of Triethylamine," *IEEE Journal on Flexible Electronics*, vol. 3, no. 3, pp. 90-99, 2024
- [9] J. H. Lee, K. Cho, and J. K. Kim, "Age of Flexible Electronics: Emerging Trends in Soft Multifunctional Sensors," *Adv Mater*, vol. 36, no. 16, p. e2310505, Apr 2024
- [10] L. Kong *et al.*, "Wireless Technologies in Flexible and Wearable Sensing: From Materials Design, System Integration to Applications," *Adv Mater*, vol. 36, no. 27, p. e2400333, Jul 2024
- [11] E. Altinozen, I. Harrison, A. Vukovic, and P. Sewell, "Systematic generation of arbitrary antenna geometries," *IEEE Transactions on Antennas and Propagation*, 2021. [Online]. Available: https://nottingham-repository.worktribe.com/output/7022934.

- [12] E. Altinozen, A. Vukovic, and P. Sewell, "Impact of Torsion on Flexible Interconnects," in 2022 IEEE International Conference on Flexible and Printable Sensors and Systems (FLEPS), 10-13 July 2022 2022, pp. 1-4,
- [13] J. Suikkola *et al.*, "Screen-Printing Fabrication and Characterization of Stretchable Electronics," *Sci Rep*, vol. 6, p. 25784, May 13 2016
- [14] D. Brosteaux, A. Fabrice, M. Gonzalez, and J. Vanfleteren, "Design and Fabrication of Elastic Interconnections for Stretchable Electronic Circuits," *IEEE Electron Device Letters*, vol. 28, no. 7, pp. 552-554, 2007.
- [15] D. M. Pozar, Microwave Engineering, 4th ed. Hoboken, N.J.: Wiley, 2012.
- [16] T. Dimitrijevic, A. Vukovic, A. Atanaskovic, J. Jokovic, P. Sewell, and N. S. Dončov, "Holistic Analysis of Conformal Antennas Using the Cylindrical TLM Method," *IEEE Transactions on Antennas and Propagation*, vol. 71, no. 5, pp. 4028-4035, 2023.
- [17] A. Vukovic, P. Sewell, and T. M. Benson, "Holistic Appraisal of Modeling Installed Antennas for Aerospace Applications," *IEEE Transactions on Antennas and Propagation*, vol. 67, no. 3, pp. 1396-1409, 2019.
- [18] E. Altinozen, I. Harrison, A. Vukovic, and P. D. Sewell, "Green Coordinates for Generation of Conformal Antenna Geometries," in 2020 14th European Conference on Antennas and Propagation (EuCAP), 15-20 March 2020 2020, pp. 1-5,
- [19] E. Altinozen, A. Vukovic, and P. Sewell, "Characterization of Flexible Interconnects," in 2022 Microwave Mediterranean Symposium (MMS), 9-13 May 2022 2022, pp. 1-4
- [20] E. Altinozen, A. Vukovic, and P. Sewell, "Assessment of the Robustness of Flexible Antennas to Complex Deformations," *IEEE Transactions on Antennas and Propagation*, vol. 71, no. 6, pp. 4714-4723, 2023.
- [21] E. Altinozen, A. Vukovic, and P. Sewell, "Assessing the Impact of Twisting and Bending Deformations on Flexible Interconnect Performance," *IEEE Journal on Flexible Electronics*, vol. 2, no. 2, pp. 233-239, 2023
- [22] P. Sewell, J. G. Wykes, T. M. Benson, C. Christopoulos, D. W. P. Thomas, and A. Vukovic, "Transmission-line modeling using unstructured triangular meshes," *IEEE Transactions on Microwave Theory and Techniques*, vol. 52, no. 5, pp. 1490-1497, 2004
- [23] P. Sewell, T. M. Benson, C. Christopoulos, D. W. P. Thomas, A. Vukovic, and J. G. Wykes, "Transmission-line Modeling (TLM) Based upon Unstructured Tetrahedral Meshes," *IEEE Transactions on Microwave Theory and Techniques*, vol. 53, no. 6, pp. 1919-1928, 2005
- [24] J.-M. Jin, *The finite element method in electromagnetics / Jian-Ming Jin*, 3rd ed. ed. Hoboken. N.J.: Hoboken. N.J.: Wiley, 2014.
- [25] A. Taflove, Computational electrodynamics: the finite-difference time-domain method / Allen Taflove, Susan C. Hagness, 3rd ed. ed. Boston [Mass.] London: Boston Mass. London: Artech House, 2005.
- [26] R. A. Liyakath, A. Takshi, and G. Mumcu, "Multilayer Stretchable Conductors on Polymer Substrates for Conformal and Reconfigurable Antennas," *IEEE Antennas and Wireless Propagation Letters*, vol. 12, pp. 603-606, 2013.
- [27] N. J. Farcich, J. Salonen, and P. M. Asbeck, "Single-Length Method Used to Determine the Dielectric Constant of Polydimethylsiloxane," *IEEE Transactions on Microwave Theory and Techniques*, vol. 56, no. 12, pp. 2963-2971, 2008.
- [28] A. S. M. Alqadami, M. F. Jamlos, P. J. Soh, and G. A. E. Vandenbosch, "Assessment of PDMS Technology in a MIMO Antenna Array," *IEEE Antennas and Wireless Propagation Letters*, vol. 15, pp. 1939-1942, 2016.
- [29] Ekmekçi E. and E. Z., "Mikrodalga ve terahertz bölgelerinde metamalzeme tabanlı özgün sensörler: tasarım, üretim ve çeşitli sensör uygulamalarında kullanılması," in "Tübitak 3501," TRDizin, 2016.



© Author(s) 2025. This work is distributed under https://creativecommons.org/licenses/by-sa/4.0/